

CAMME: Adaptive Deepfake Image Detection with Multi-Modal Cross-Attention

Naseem Khan¹, Tuan Nguyen², Amine Bermak¹, Issa Khalil²
¹Hamad Bin Khalifa University (HBKU), Qatar
²Qatar Computing Research Institute (QCRI), HBKU, Qatar

Abstract

The proliferation of sophisticated AI-generated deepfakes poses critical challenges for digital media authentication and societal security. While existing detection methods perform well within specific generative domains, they exhibit significant performance degradation when applied to manipulations produced by unseen architectures—a fundamental limitation as generative technologies rapidly evolve. We propose CAMME (Cross-Attention Multi-Modal Embeddings), a framework that dynamically integrates visual, textual, and frequency-domain features through a multi-head cross-attention mechanism to establish robust cross-domain generalization. Extensive experiments demonstrate CAMME’s superiority over state-of-the-art methods, yielding improvements of 12.56% on natural scenes and 13.25% on facial deepfakes. The framework demonstrates exceptional resilience, maintaining (over 91%) accuracy under natural image perturbations and achieving 89.01% and 96.14% accuracy against PGD and FGSM adversarial attacks, respectively. Our findings validate that integrating complementary modalities through cross-attention enables more effective decision boundary realignment for reliable deepfake detection across heterogeneous generative architectures.

1 Introduction

The rise of deepfake technology—capable of synthesizing highly realistic, AI-generated static images—poses a profound challenge to digital media integrity. Leveraging Generative Artificial Intelligence (GAI), such as Stable Diffusion [1], DALL-E [2], StyleCLIP [3], and Imagen [4], malicious actors can produce fabricated images that are nearly indistinguishable from real photographs. These images enable the spread of misinformation (e.g., fake news imagery), identity fraud, and unauthorized replication of artistic styles, raising ethical concerns about privacy, copyright, and originality

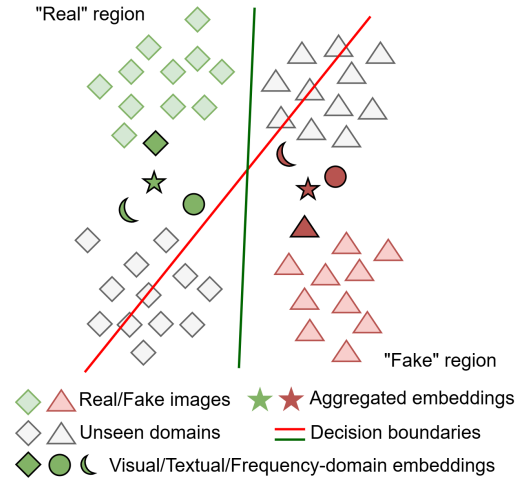


Figure 1: Challenges in detecting unseen domains. Traditional deepfake detection methods usually rely on uni-modal embeddings (e.g., visual embeddings), resulting in non-generalizable decision boundaries (red line) that struggle with unseen domains (grey examples). Unlike previous approaches, our framework aggregates information from visual, text, and frequency domains to re-align the decision boundary (green line), enhancing transferability to unseen target domains.

[5, 6, 7, 8, 9, 10]. As GAI continues to evolve, the urgency for effective deepfake detection mechanisms grows.

Current detection methods excel in **intra-domain** settings, where training and testing occur within the same generative architecture (e.g., GAN-based models). However, real-world deepfakes often stem from diverse generative models, introducing significant distribution shifts that impair performance in **inter-domain** scenarios. As illustrated in Figure 1, this challenge manifests in two critical ways: visually, through decision boundaries (red line) that fail to classify unseen samples correctly, and quantitatively, through se-

Table 1: Cross-domain transferability analysis: F1 scores (%) for intra-domain and inter-domain evaluations. $X \rightarrow Y$ represents training on domain X and testing on domain Y , where G: GLIDE, V: VQDM.

Methods	G→G	G→V	V→V	V→G
DE-FAKE [11]	98.86	34.42	95.45	51.40
UnivCLIP [12]	97.63	28.57	97.39	43.04
UnivConv2B [13]	99.97	33.17	99.76	78.70
DCT [14]	99.20	45.84	97.32	64.45

vere performance degradation when models are evaluated across domains. The F1 scores presented in Table 1 reveal that state-of-the-art methods experience dramatic accuracy drops in cross-domain settings, with performance deteriorating from over 95% to below 50% when training on one generative architecture (e.g., GLIDE) and testing on another (e.g., VQDM). This evidence underscores the urgent need for detection frameworks capable of generalizing across heterogeneous generative architectures.

We propose **CAMME** (Cross-Attention Multi-Modal Embeddings), a novel framework to enhance cross-domain transferability in deepfake image detection. CAMME integrates three modalities—visual embeddings for semantic content [12], textual embeddings for contextual consistency [11], and frequency-domain features for spectral artifacts [14]—to construct a robust feature space. A multi-head cross-attention mechanism, inspired by [15], dynamically weights these modalities, enabling adaptive focus on the most discriminative features for a given image. This approach facilitates flexible decision boundary adjustments, improving generalization to unseen domains and resilience against perturbations.

Our contributions are:

- We introduce CAMME, a multi-modal cross-attention framework that enhances deepfake detection transferability across generative domains, improving state-of-the-art performance by over 12%.
- We develop a multi-modal benchmark by augmenting selected images from GenImage [16] with BLIP-generated captions, creating a dataset of 161,837 natural scene images across five generative architectures. We also compile 100,000 facial images for comprehensive cross-domain evaluation.
- We demonstrate CAMME’s exceptional robustness, maintaining over 91% accuracy under natural perturbations and 89%–96% accuracy against adversarial attacks (PGD, FGSM).

These advancements mark a significant step toward

reliable deepfake detection in an era of diverse GAI technologies. Our code and datasets are available at: <https://github.com/Magnet300/CAMME.git>.

2 Related Work

Deepfake image detection has emerged as a critical area of research due to its implications for privacy and societal security [17, 18, 19]. We review relevant approaches and their limitations, focusing particularly on two fundamental challenges: cross-domain generalization capabilities and robustness against both natural and adversarial perturbations.

2.1 Evolution of Deepfake Detection Methods

Early deepfake detection relied on handcrafted feature-based methods that identified distinctive generation artifacts through preprocessing techniques [20, 21]. These approaches typically employed classical machine learning algorithms such as SVMs [22], Random Forests [23], and MLPs [24] for classification. However, these methods generally exhibit limited adaptability to novel generation techniques and poor cross-domain generalization [19].

In contrast, deep feature-based methods offer more robust performance by learning representations directly from data, capturing high-level spatial patterns that adapt more effectively across different deepfake generation techniques [25, 26]. Recent state-of-the-art approaches have further enhanced detection performance by leveraging uni-modal information sources, including visual, textual, and frequency domains [13, 12, 14, 11].

2.2 Uni-Modal Approaches and Their Limitations

Recent deepfake detection methods can be categorized based on their primary feature domain. Visual embedding-based approaches like UnivCLIP [12] leverage CLIP [27] to extract semantic representations, measuring distances between image embeddings for classification. While effective within domains, these approaches struggle with cross-domain generalization due to their limited ability to identify subtle artifacts across different generative architectures.

Text-augmented approaches such as DE-FAKE [11] combine visual and textual embeddings using CLIP and caption generation models like BLIP [28]. These methods exploit the observation that real images typically contain more diverse and informative content

than synthetic images generated from simpler prompts. However, they remain vulnerable to sophisticated generations that closely match prompt descriptions.

Frequency-domain methods like DCT [14] focus on spectral artifacts, especially useful for detecting diffusion model outputs that exhibit fewer spatial anomalies than GAN-generated images. By applying logarithmic Discrete Cosine Transform analysis, these approaches have demonstrated significant improvements (16.3%) over visual-only methods. Nevertheless, they often lack robustness against adversarial attacks that specifically target frequency patterns.

Comprehensive approaches like UnivConv2B [13] have analyzed trade-offs between generalization performance and adversarial robustness. Their findings reveal that frequency-domain models excel in generalization but remain vulnerable to adversarial manipulation, while visual feature-based models show greater resilience against attacks at the cost of reduced cross-domain transferability.

2.3 Watermarking vs. Artifact-Based Detection

An alternative to artifact detection is watermarking [29, 30, 31, 32, 33], which embeds imperceptible patterns during image creation for later verification. However, watermarking approaches face significant limitations: vulnerability to common image processing operations (resizing, transcoding, filtering), susceptibility to manipulation by advanced AI tools, image quality degradation, and challenges in balancing robustness with imperceptibility.

2.4 Motivation for Multi-Modal Approach

Our analysis of existing uni-modal approaches reveals a critical gap: while each domain (visual, textual, frequency) provides valuable detection signals, none alone achieves both strong cross-domain generalization and robust adversarial defense. As demonstrated in Figure 1, state-of-the-art methods exhibit severe performance collapse ($> 60\%$ F1-score drop) when evaluated across different generative domains. This limitation motivates our multi-modal framework, which integrates complementary features through cross-attention mechanisms to dynamically adjust decision boundaries, addressing fundamental generalization challenges in deepfake detection.

3 Background

3.1 Generative Models

Generative Adversarial Networks (GANs) [34, 35, 36, 37] were initially developed to synthesize images by learning a distribution that closely mimics that of real data. GANs have since been widely adopted across various applications, particularly for image generation. However, GAN-based models often face challenges in producing realistic images due to issues like training instability and mode collapse, where the generator fails to capture the full diversity of the data. These limitations have led to the emergence of diffusion models as a preferred alternative, offering improved realism in generated images. Denoising Diffusion Probabilistic Models (DDPMs) [38] pioneered this approach, successfully generating high-quality images through a denoising diffusion process and inspiring a wide range of diffusion models [1, 39, 40, 41].

Recent advancements, such as Stable Diffusion, introduced cross-attention mechanisms between text and visual embeddings, highlighting the effectiveness of text-driven image generation by focusing on user prompts. This integration of text and image information has been further refined in the CLIP model [27], which employs a contrastive loss to align text and image embeddings. By anchoring semantic meaning to images, CLIP not only enhances zero-shot classification performance but also strengthens the connection between textual and visual modalities for diverse downstream tasks.

3.2 Transfer Learning

In this section, we introduce the framework of transfer learning for deepfake image detection. In transfer learning or domain adaptation, the objective is to adapt a model trained on one domain (referred to as the source domain) so that it performs well on a different domain (referred to as the target domain). For instance, in the context of deepfake image detection, the source domain could be a set of images generated by a GAN-based model, while the target domain could consist of images generated by an unseen diffusion-based model.

Let $\mathcal{D}^S = \{(x_i^S, y_i^S)\}_{i=1}^{N_S}$ represent the dataset of the source domain, where $x_i^S \in \mathcal{X}^S$ denotes the input features and $y_i^S \in \mathcal{Y}$ denotes the labels. In deep fake detection, $y_i = 0$ represents the *real* class, and $y_i = 1$ represents the *fake* class. The dataset for the target domain is denoted by $\mathcal{D}^T = \{x_i^T\}_{i=1}^{N_T}$. Note that the target domain remains entirely unseen and unlabeled during training.

Our primary objective is to learn a mapping $f : \mathcal{X} \rightarrow \mathcal{Y}$ that generalizes well on the source domain and performs robustly on the unseen target domain:

$$\min_f \mathbb{E}_{(x,y) \sim P^T} [\mathcal{L}(f(x), y)], \quad (1)$$

where P^T represents the distribution over the target domain, and \mathcal{L} is the loss function (e.g., cross-entropy loss). However, in this context, we do not have access to labeled target data during training, so we cannot directly minimize the above objective. Instead, we approximate the mapping f by minimizing the loss over the source domain distribution P^S , where labeled data is available:

$$\min_f \mathbb{E}_{(x,y) \sim P^S} [\mathcal{L}(f(x), y)]. \quad (2)$$

In practice, f can be decomposed as $f = h \circ G$, where $G : \mathcal{X} \rightarrow \mathcal{Z}$ maps the input x to a feature space \mathcal{Z} (referred to as the feature extractor), and $h : \mathcal{Z} \rightarrow \mathcal{Y}$ maps from the feature space to the final output in \mathcal{Y} (referred to as the classifier). The objective in Equation (2) can then be rewritten as:

$$\min_{G,h} \mathbb{E}_{(x,y) \sim P^S} [\mathcal{L}(h(G(x)), y)]. \quad (3)$$

3.3 Discrete Cosine Transform

The Discrete Cosine Transform (DCT) is widely used in image processing and computer vision tasks due to its ability to capture frequency components effectively [42, 43, 44]. An image I can be transformed into its DCT representation F using the following equation:

$$F_{k,l} = \sum_{m=0}^{M-1} \sum_{n=0}^{N-1} I_{m,n} C_M(m, k) C_N(n, l), \quad (4)$$

where

$$C_M(m, k) = \cos\left(\frac{\pi}{M} \left(m + \frac{1}{2}\right) k\right), \quad (5)$$

$$C_N(n, l) = \cos\left(\frac{\pi}{N} \left(n + \frac{1}{2}\right) l\right). \quad (6)$$

Here, $F_{k,l}$ represents the DCT coefficient at row k and column l of the DCT matrix, while $I_{m,n}$ denotes the pixel value at row m and column n in the image. The DCT coefficients capture various frequency components of the image, with *lower frequencies* concentrated in the top-left corner of the DCT matrix and *higher frequencies* towards the bottom-right. Lower frequencies correspond to smooth, gradual intensity changes (e.g., background regions), whereas higher frequencies capture rapid changes (e.g., edges and textures). This property makes DCT particularly useful

for detecting artifacts in image forensics and deepfake detection, as real and manipulated images often exhibit distinct patterns in their frequency components.

4 Our Proposed Method

4.1 Overview

In this section, we introduce our proposed method to enhance transferability in deepfake image detection. Current state-of-the-art detectors primarily rely on uni-modal embeddings, such as *image-based* [12, 13] or *frequency-based* modalities [14], each offering distinct advantages. For instance, an analysis in [13] indicates that frequency-domain-based models exhibit strong generalization, whereas models based on visual features demonstrate greater resilience to adversarial manipulations. The main challenge lies in integrating these uni-modal embeddings to enhance generalization and transferability across diverse domains, while preserving the unique benefits of each embedding type. Furthermore, connecting embeddings from different spaces is complex, as each type (e.g., visual, textual, and frequency-domain) has distinct characteristics and representations. Motivated by this challenge, we propose a multi-modal deepfake detection method that integrates visual, textual, and frequency-domain features, leveraging the strengths of these uni-modal embeddings through a cross-attention mechanism. Our approach, named **CAMME** (Cross-Attention on Multi-Modal Embedding), is designed to enhance deepfake detection capabilities and improve model transferability across diverse domains.

4.2 Modality Embedding Extraction

In what follows, we describe the feature extraction process for visual, text, and frequency-domain embeddings.

Visual Embeddings. Rather than designing vision models from scratch, we leverage pre-trained visual models trained on large-scale datasets. These models learn highly generalizable representations, producing rich features suitable for downstream tasks such as image classification. For our visual feature extraction, we adopt OpenCLIP-ConvNextLarge [45], following established baselines [13] for feature extractors.

Text Embeddings. Real images typically contain richer semantic content than the prompts used to generate fake images, which are often derived from simpler prompts. Based on this observation, [11] demonstrates that textual information can help distinguish between real and fake images. In this work, we utilize CLIP’s text encoder to extract embeddings from

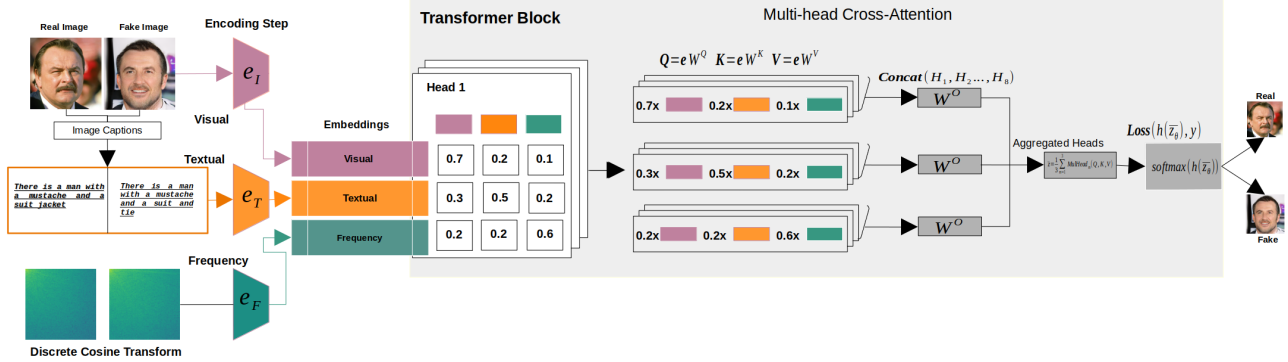


Figure 2: CAMME framework: A multi-modal transformer architecture for deepfake detection. Images are encoded into visual, textual, and frequency domain embeddings, which are treated as sequential tokens. The transformer block applies self-attention across these tokens, enabling cross-modal interactions. Each attention head dynamically weights features from different modalities. The final representation is obtained by weighted aggregation of the attention outputs for binary classification. The model effectively captures complementary discriminative features across domains.

image prompts. For datasets lacking prompt information, we employ BLIP [28] to generate captions for the images, making this approach applicable to real-world scenarios where associated text may be unavailable.

Frequency-Domain Embeddings. Detecting fake images in the frequency domain has shown potential, as generated images often display differences (e.g., artifacts) from real images. Inspired by [14], we apply the Discrete Cosine Transform (DCT) to extract frequency-domain features from images, as described in Equation (4). These frequency-based features capture artifacts that may be indicative of image manipulation.

4.3 Multi-head Cross Attention Mechanism

To find the optimal solution for Equation (3), we first extract visual, textual, and frequency-domain embeddings from the input images:

$$\mathbf{e}_I = G_I(x), \quad \mathbf{e}_T = G_T(x), \quad \mathbf{e}_F = G_F(x), \quad (7)$$

where G_I, G_T, G_F denote the feature extractors for visual, textual, and frequency-domain embeddings, respectively. These embeddings raise the critical question of how to effectively integrate them to enhance model generalization. Various techniques, such as element-wise addition, concatenation, average pooling, or learnable weighted averaging, can be applied to combine these embeddings. However, as shown in our experiments (Section 5.4.1), these methods may not fully capture the interactions among embeddings. Additionally, the model’s performance may depend on the

type of information needed for each detection. For instance, “easy” fake images, such as those generated by GAN-based models, are often distinguishable using frequency-domain features alone [14], whereas “harder” examples may require multi-modal information for accurate detection. Therefore, the model’s detection performance is highly dependent on its ability to selectively focus on relevant information from each embedding type.

Inspired by this insight, we propose a cross-attention mechanism to strengthen the interactions among uni-modal embeddings and enable the model to focus on the most relevant information for each decision. Under the framework of the multi-head self-attention architecture [15], we treat each uni-modal embedding as a *token* in a sequence to apply attention across these uni-modal tokens. This viewpoint maintains flexibility, enabling our model to be extended to more than three modalities, such as visual, text, frequency, audio, sensor, or graph data, by treating each modality as a distinct token in the sequence. In this framework, let \mathbf{e} represent a sequence of three token embeddings:

$$\mathbf{e} = \{\mathbf{e}_I, \mathbf{e}_T, \mathbf{e}_F\} \in \mathbb{R}^{3 \times d_e}. \quad (8)$$

We then project \mathbf{e} into query (Q), key (K), and value (V) matrices as follows:

$$Q = \mathbf{e}W^Q, \quad K = \mathbf{e}W^K, \quad V = \mathbf{e}W^V, \quad (9)$$

where $Q \in \mathbb{R}^{3 \times d_k}$, $K \in \mathbb{R}^{3 \times d_k}$, and $V \in \mathbb{R}^{3 \times d_v}$.

The self-attention mechanism [15] is applied to Q , K , and V , with the attention score computed as:

$$\text{Attention}(Q, K, V) = \text{softmax}\left(\frac{QK^\top}{\sqrt{d_k}}\right)V. \quad (10)$$

Here, QK^\top measures the similarity between token embeddings in \mathbf{e} . Thus, *the self-attention mechanism applied to \mathbf{e} acts as a form of cross-attention across the visual, text, and frequency-domain embeddings*. In multi-head attention, we concatenate the outputs of multiple attention heads and project them back to the original embedding dimension. Let $h_i = \text{head}_i$ and $\text{MH} = \text{MultiHead}$ for brevity:

$$h_i = \text{Attention}(Q_i, K_i, V_i), \quad (11)$$

$$\text{MH}(Q, K, V) = \text{Concat}(h_1, \dots, h_H)W^O \quad (12)$$

where $h_i \in \mathbb{R}^{3 \times d_v}$, $W^O \in \mathbb{R}^{Hd_v \times d_e}$ is the output projection matrix, and H is the number of heads. This yields $\text{MH}(Q, K, V) \in \mathbb{R}^{3 \times d_e}$. The output of the multi-head attention is then aggregated into a single embedding that captures the interactions among the visual, text, and frequency-domain embeddings:

$$\bar{z} = \frac{1}{3} \sum_{m=1}^3 \text{MH}_m(Q, K, V). \quad (13)$$

4.4 Training Objective

The aggregated embedding \bar{z} is subsequently fed into a classifier h to predict the probability that the input image is real or fake. The optimization problem in Equation (3) is then reformulated as:

$$\min_{\theta, h} \mathbb{E}_{(x, y) \sim \mathcal{P}^S} [\mathcal{L}(h(\bar{z}_\theta), y)], \quad (14)$$

where $\theta = \{W_i^Q, W_i^K, W_i^V, W^O\}$ are the learnable parameters in the multi-head attention module. Details of the training process are provided in Section 5.2. Figure 2 illustrates our proposed framework for deepfake image detection.

5 Experiment

In this section, we present our data collection and experimental results on natural scene and face datasets.

5.1 Dataset Construction

5.1.1 Natural Scene Dataset

To evaluate the transferability of our model, we follow the approach in [16] to construct a dataset using images generated by popular generative models, including Stable Diffusion V1.5 [1], ADM [39], GLIDE [40], VQDM

[41], and BigGAN [37]. The authors generated synthetic images using pre-trained models with prompts in the format “photo of [class name]”, where “[class name]” is replaced with ImageNet labels. We collect in total 161,837 images from these models.

Following the procedure outlined in [13], we split each dataset into training, validation, and test sets with an 80 : 10 : 10 ratio. The dataset is balanced, containing an equal number of real and fake images. Each dataset includes 100 categories, specifically the first 100 categories from ImageNet [46]. With around 320 images per category, this dataset poses a significant challenge for any deepfake detection method to generalize effectively across unseen domains.

5.1.2 Face Dataset

The face dataset is based on the dataset introduced in [47]. Real images are sourced from CelebA [48], CelebA-HQ [36], and Youtube-Frame [49], while fake images are generated using PGGAN [36], Glow [50], Face2Face [51], and StarGAN [35]. To represent the face domain comprehensively, we create the following combined subsets: (i) CelebA-HQ paired with PGGAN (CelPG); (ii) CelebA with StarGAN (CelStar); (iii) CelebA with Glow (CelGlow); and (iv) Youtube-Frame with Face2Face (YouFace). These combinations align the properties of real and synthetic images within each subset, enabling meaningful comparisons between real and fake classes. For each dataset, we collect 20,000 images, consisting of 10,000 real and 10,000 fake images, resulting in a total of 100,000 images for the face dataset.

The natural scene and face datasets encompass a diverse range of generative models and content types, making them representative of real-world deepfake challenges. The Natural Scene Dataset captures variability across generative architectures, with models producing highly realistic images that are challenging to detect due to subtle artifacts. The Face Dataset includes both unaltered and manipulated faces, representing common deepfake targets such as identity swapping and attribute editing. These datasets were selected to address key challenges: generalization to unseen deepfakes, robustness against high-quality manipulations, and adaptation to diverse content types. Together, they provide a comprehensive benchmark for advancing deepfake detection methods and tackling future challenges posed by increasingly sophisticated deepfakes. The two datasets collectively comprise 261,837 images. Appendix A provides further details on the composition and distribution of the datasets, along with illustrative examples of real and fake images from each dataset (Figures 4).

Table 2: F1 score (%) for detection performance on the natural scene dataset. Bold blue text indicates intra-domain performance. The highest score is shown in bold black, and the second-highest is underlined.

Methods	Target	SD V1.5	ADM	GLIDE	VQDM	BigGAN	Inter-domain Average (IA)	Average of IA
	Source							
DE-FAKE	SD V1.5	98.62	1.96	52.34	22.06	7.39	20.94	33.29
	ADM	1.86	98.53	13.83	04.53	27.92	12.04	
	GLIDE	42.89	28.47	98.86	34.42	94.74	50.13	
	VQDM	34.64	23.16	51.40	95.45	78.32	46.88	
	BigGAN	4.05	26.71	93.70	21.31	99.62	36.44	
UnivCLIP	SD V1.5	97.41	7.09	65.55	14.60	34.93	30.54	41.53
	ADM	10.27	92.76	71.13	93.89	83.76	64.76	
	GLIDE	41.45	27.15	97.63	28.57	56.93	38.53	
	VQDM	16.96	53.79	43.04	97.39	88.33	50.53	
	BigGAN	2.54	9.55	22.96	58.02	99.09	23.27	
UnivConv2B	SD V1.5	99.86	0.12	12.86	01.52	4.60	4.78	39.71
	ADM	0.78	99.71	99.12	98.91	99.74	<u>74.64</u>	
	GLIDE	1.12	24.38	99.97	33.17	70.87	32.39	
	VQDM	4.49	90.28	78.70	99.76	95.57	67.26	
	BigGAN	2.66	10.52	24.65	40.06	99.94	19.47	
DCT	SD V1.5	96.74	46.52	63.11	90.27	52.86	<u>63.19</u>	<u>65.15</u>
	ADM	72.17	99.20	63.42	72.64	51.27	64.88	
	GLIDE	50.68	51.07	99.20	45.84	72.19	<u>54.95</u>	
	VQDM	86.01	73.71	64.45	97.32	72.74	<u>74.23</u>	
	BigGAN	57.04	63.06	96.74	57.19	100.00	68.51	
CAMME (Ours)	SD V1.5	99.49	66.47	74.76	68.35	72.03	70.40 (+7.21)	77.71 (+12.56)
	ADM	66.19	99.47	95.65	98.97	99.26	90.02 (+15.38)	
	GLIDE	66.94	69.35	99.65	73.41	74.12	70.96 (+16.01)	
	VQDM	66.73	94.12	84.60	99.79	92.39	84.46 (+10.23)	
	BigGAN	67.08	70.48	74.94	78.40	99.76	72.73 (+4.22)	

5.2 Implementation Details

5.2.1 Training

Images are preprocessed and resized to 320×320 to match the input requirements of the pretrained OpenCLIP-ConvNextLarge model [27]. Text prompts are also processed through the same pretrained model to obtain text embeddings. Frequency features are extracted by applying the Discrete Cosine Transform (DCT) to the images, following [13, 14], where we compute the logarithm of the absolute values of the DCT coefficients to capture frequency-domain characteristics. The DCT features are then normalized by subtracting the mean and dividing by the standard deviation, followed by a linear transformation to match the dimension of the visual and text embeddings.

At the end of the feature extraction process, we obtain three embeddings—visual, text, and frequency-domain—with a unified dimension of $d_e = 768$. These

uni-modal embeddings are subsequently fed into the multi-head cross-attention module with 8 heads, where the dimensions of Q , K , and V are set to $d_k = d_v = 96$. The model computes attention scores using scaled dot-product attention to capture cross-modal relationships. After applying softmax to obtain attention weights, these weights are used to compute a weighted average of the value V , effectively integrating information across domains. The outputs from each head are concatenated and averaged to produce the aggregated embedding, which is expected to capture diverse interactions among visual, text, and frequency-domain features. Finally, this aggregated embedding is passed through a classifier to predict whether the input image is real or fake. The model is trained by minimizing the loss in Equation (14) using backpropagation. For fair comparison with baseline implementations in [13, 12], we freeze the pretrained visual and text embeddings from OpenCLIP-ConvNextLarge during training.

For the baseline models, we use the authors’ offi-

cial code repositories and evaluate these methods on our dataset with the same hyperparameters specified in their original implementations. For our proposed method, we use a batch size of 128 and the Adam optimizer [52] with a learning rate of 0.001. Training is conducted for 30 epochs with early stopping based on validation loss. All experiments are conducted on 8 Tesla V100-SXM2 GPUs with 32GB of memory each.

5.2.2 Evaluation

The evaluation is performed on the test set, with Precision, Recall, F1 score, and Accuracy reported as evaluation metrics. For consistency, F1 scores for the Natural Scene and Face datasets are provided in Table 2 and Table 3, respectively, as F1 offers a balanced metric between Precision and Recall. Detailed results for Precision, Recall, F1, and Accuracy are presented in Appendix B.

We also report intra-domain performance in the tables, representing the model’s performance within the same domain. Additionally, the Inter-domain Average (IA) is calculated as the average of all inter-domain transfer tasks (where the source and target domains differ) to measure model performance on unseen domains. The overall transferability performance of the model on unseen datasets is represented by the Average of IA.

5.3 Results and Discussion

5.3.1 Natural Scene Dataset

Baseline methods such as DE-FAKE, UnivConv2B, and DCT perform well in source-only settings, where the model is trained and evaluated on the same dataset (e.g., SD V1.5 → SD V1.5, ADM → ADM). DCT, in particular, achieves strong results, correctly identifying BigGAN images with 100% accuracy. However, these methods exhibit a substantial drop in average F1 scores when applied to unseen target domains. For instance, when detecting fake images from an unseen model after training on SD V1.5, DE-FAKE averages an F1 score of 20.94%, while UnivCLIP achieves 30.54%.

In contrast, our proposed CAMME achieves the highest inter-domain average F1 score across all source-target combinations, with improvements of 7.21% when trained on SD V1.5, 15.38% when trained on ADM, and a significant increase of 16.0.1% when trained on GLIDE. Furthermore, when trained on VQDM and BigGAN, CAMME surpasses DCT by 10.23% and 4.22%, respectively. These gains are driven by CAMME’s multimodal design, which goes beyond frequency patterns to integrate visual and text-based features, enabling a more nuanced understanding of the

data. This results in greater cross-domain resilience compared to single-modal methods like UnivCLIP and DCT, enhancing CAMME’s transferability and generalization performance on unseen target domains. Overall, when averaging across all transfer tasks (last column), CAMME achieves an F1 score of 77.71%, outperforming the next best method, DCT, by 12.56%.

5.3.2 Face Dataset

The baseline methods show poor performance on unseen domains (inter-domain), with DE-FAKE achieving an average F1 score of only 23.97% on CelPG, 2.67% on CelStar, and just 0.5% on CelGlow. UnivCLIP performs well in source-only (intra-domain) settings (e.g., 98.06% on CelGlow) but suffers a significant drop in average cross-domain (inter-domain) scores (e.g., an inter-domain F1 score of 36.77% on CelGlow). DCT achieves competitive results on intra-domain settings, such as 99.95% on CelStar, due to its frequency-based analysis; however, it underperforms in domains requiring visual-semantic understanding, trailing CAMME on complex datasets like YouFace. The YouFace dataset combines real images with varying lighting, poses, and expressions from YouTube-Frame, along with advanced reenactment manipulations from Face2Face, posing unique challenges for frequency-focused methods like DCT.

In contrast, CAMME consistently outperforms the baselines in inter-domain tasks, achieving top average F1 scores of 69.36% on CelPG, 66.67% on CelStar, and 66.62% on CelGlow, representing an improvement of 27.21% over the current state-of-the-art method. Single-modal methods such as UnivConv2B and DCT also struggle with the subtle generative artifacts introduced by StarGAN [35] and Face2Face [51]. Specifically, UnivConv2B and DCT attain 0% and 49.01% on CelStar, and 40.35% and 60.61% on YouFace, respectively. The overall performance of the proposed CAMME, averaged across all tasks (last column), is 66.46%, surpassing the next best method, UnivCLIP, by 13.25%.

In the last row of Table 3, we present the results of training on the YouFace dataset as the source domain. The findings indicate that the model trained on YouFace performs worse than the current baseline. Upon further analysis, we identified an issue originating from the prompt generation step of BLIP [28]. Specifically, in the YouTube-Frame dataset, many frames are derived from the same individual, yet the BLIP model generates prompts describing entirely unrelated objects. This mismatch causes inaccurate semantic representations in the text embeddings, confusing the model and degrading performance on other

Table 3: F1 score (%) for detection performance on the face dataset (Simplified). Bold blue text indicates intra-domain performance. The highest score is shown in bold black, and the second-highest is underlined.

Methods	Target		CelPG	CelStar	CelGlow	YouFace	Inter-domain Average (IA)	Average of IA
	Source							
DE-FAKE	CelPG	95.91	63.30	7.03	1.59	23.97	15.98	
	CelStar	2.37	99.85	5.63	0.00	2.67		
	CelGlow	0.00	0.40	99.24	1.09	0.5		
	YouFace	67.00	39.49	3.89	80.72	36.79		
UnivCLIP	CelPG	99.60	92.28	31.74	58.21	60.74	<u>53.21</u>	
	CelStar	77.03	99.25	6.00	40.73	41.25		
	CelGlow	6.73	72.03	98.08	31.55	36.77		
	YouFace	93.31	87.44	41.47	92.81	74.07		
UnivConv2B	CelPG	99.90	78.80	14.14	30.55	41.16	28.94	
	CelStar	0.00	99.95	0.00	0.00	0.00		
	CelGlow	0.79	67.29	100.00	34.66	34.25		
	YouFace	79.90	13.81	27.35	98.27	40.35		
DCT	CelPG	92.42	9.14	41.49	38.04	29.56	44.65	
	CelStar	34.85	99.95	54.26	57.93	<u>49.01</u>		
	CelGlow	44.59	20.21	99.35	53.43	<u>39.41</u>		
	YouFace	55.68	76.10	50.05	75.72	60.61		
CAMME (Ours)	CelPG	99.75	75.17	62.24	70.67	69.36 (+8.62)	66.46 (+13.25)	
	CelStar	66.69	100.00	66.73	66.60	66.67 (+17.66)		
	CelGlow	66.78	77.35	99.95	55.74	66.62 (+27.21)		
	YouFace	69.34	54.68	55.40	95.32	<u>63.19</u>		

datasets. Further analysis and examples of these failures are in Appendix C.

5.4 Analysis

5.4.1 Embedding Combination Methods

We evaluate different strategies for combining visual, textual, and frequency embeddings in our proposed method. Specifically, we compare the performance of the following five approaches:

- Element-wise Addition*: The embeddings are combined by summing them element-wise: $\bar{\mathbf{e}} = \mathbf{e}_I + \mathbf{e}_T + \mathbf{e}_F$.
- Concatenation*: The embeddings are concatenated along the channel dimension: $\bar{\mathbf{e}} = [\mathbf{e}_I, \mathbf{e}_T, \mathbf{e}_F]$.
- Average Pooling*: The embeddings are combined by averaging their values across the channel dimension: $\bar{\mathbf{e}} = \frac{1}{3}(\mathbf{e}_I + \mathbf{e}_T + \mathbf{e}_F)$.
- Learnable Weighted Average*: Trainable weights $\mathbf{w} \in \mathbb{R}^{1 \times 3}$ are initialized, scaled via the softmax function, and learned during training: $\bar{\mathbf{e}} = \text{softmax}(\mathbf{w}) \cdot [\mathbf{e}_I, \mathbf{e}_T, \mathbf{e}_F]$.

- Multi-Head Cross-Attention*: Our proposed method, which uses a cross-attention mechanism to dynamically aggregate information from the embeddings.

For methods (a), (b), (c), and (d), we then apply a linear layer to the combined embedding $\bar{\mathbf{e}}$ for classification. The experimental results are presented in Table 4.

Our proposed model (CAMME) with multi-head cross-attention achieves the highest average F1 score of 81.63%, outperforming the second-best method, *Learnable Weighted Average*, by 8.05%. This result demonstrates the effectiveness of our method, showing that even a single-head configuration can capture interactions between different embeddings and leverage their complementary information to enhance deepfake detection performance.

5.4.2 Input Embedding Scenario Analysis

In this section, we investigate the impact of different input embeddings on the performance of the cross-attention mechanism. Specifically, we omit one token embedding from \mathbf{e} in Equation (8) and conduct exper-

Table 4: Ablation study of different embedding aggregation methods (intra-domain performance shown in bold blue text).

Methods	Target		SD V1.5	ADM	GLIDE	VQDM	BigGAN	Inter-domain Average (IA)	Average of IA
	Source								
Element-wise Addition	SD V1.5		88.76	71.61	73.75	69.21	86.20	77.71	56.53
	ADM		67.11	98.09	65.98	94.83	65.46	58.68	
	VQDM		66.39	86.75	66.12	98.54	65.53	33.20	
Concatenation	SD V1.5		86.82	72.61	62.75	69.74	80.33	71.36	71.57
	ADM		66.25	97.53	65.42	94.02	65.18	72.72	
	VQDM		66.26	84.14	66.40	98.51	65.72	70.63	
Average Pooling	SD V1.5		87.64	74.13	63.21	71.65	81.78	72.69	71.94
	ADM		64.88	94.07	65.45	94.07	64.88	72.32	
	VQDM		65.81	86.23	65.64	98.08	65.53	70.8	
Learnable Weighted Average	SD V1.5		92.87	73.87	72.76	70.66	86.07	75.84	73.58
	ADM		66.54	97.89	66.37	96.58	65.43	73.73	
	VQDM		66.04	87.36	65.96	97.90	65.27	71.16	
Multi-Head Cross-Attention	SD V1.5		99.49	66.47	74.76	68.35	72.03	70.40	81.63
	ADM		66.19	99.47	95.65	98.97	99.26	90.02	
	VQDM		66.73	94.12	84.60	99.79	92.39	84.46	

Table 5: Ablation study of different embedding combinations (intra-domain performance shown in bold blue text).

Methods	Target		SD V1.5	ADM	GLIDE	VQDM	BigGAN	Inter-domain Average (IA)	Average of IA
	Source								
Visual and Text	BigGAN		66.62	68.02	68.68	71.65	99.94	68.74	79.70
	ADM		66.35	99.44	97.97	98.85	99.41	90.65	
Visual and Frequency	BigGAN		67.58	69.10	70.29	71.07	92.32	69.51	79.42
	ADM		66.44	99.35	93.00	98.82	99.03	89.32	
Text and Frequency	BigGAN		65.13	66.22	65.35	65.88	97.48	65.65	68.78
	ADM		65.40	96.55	65.55	92.13	64.55	71.91	
Visual, Text and Frequency	BigGAN		67.08	70.48	74.94	78.40	99.76	72.73	81.38
	ADM		66.19	99.47	95.65	98.97	99.26	90.02	

iments on various scenarios: (i) *Visual and Text*, (ii) *Visual and Frequency*, (iii) *Text and Frequency*, and (iv) *Visual, Text, and Frequency* (proposed method). The results are presented in Table 5.

From the table, it is evident that excluding visual embeddings leads to significantly lower performance, as seen in the *Text and Frequency* combination, which achieves an average F1 score of 68.78%. The inclusion of frequency or text embeddings proves beneficial, particularly when combined with visual data, as demonstrated by the high scores in the *Visual and Text* (79.70%) and *Visual and Frequency* (79.42%) combinations, respectively. Our proposed method, which integrates all three embeddings, achieves the highest average F1 score of 81.38%, surpassing the second-best combination, *Visual and Text*, by 1.68%. This combination provides the model with the most comprehensive representation, capturing visual, semantic, and spectral information, which improves overall detection accuracy.

5.4.3 Natural Perturbations

This section evaluates the proposed model’s performance under traditional image transformations, including Gaussian noise, Gaussian blur, JPEG compression, sharpening, and color jittering. The GLIDE [40] dataset was chosen due to its high detection accuracy across all baselines, enabling an analysis of performance drops after applying these transformations. All test images from the test set of GLIDE were used, with hyperparameters adjusted for different intensity levels. The average F1 score was reported, as it provides a balanced measure of precision and recall. In this scenario, minimizing false negatives (fake images classified as real) and false positives (real images classified as fake) is crucial. Natural perturbations introduced by image editing tools or apps may cause misclassifications, especially if real images are mistakenly flagged as fake. Note that these transformations are not considered fake manipulations as they do not alter the intrinsic content of the images. Figure 3 illustrates an example of these perturbations before and after application. In each figure, we compute the FID score [53] to assess the quality of natural perturbations by

Table 6: Average F1 scores for varying intensities of natural perturbations on manipulated images from GLIDE dataset.

Methods (FID values)	Unperturbed	Gaus. Noise	Gaus. Blur	JPEG Comp.	Sharpening	Color Jittering
	-	2.73	4.40	3.23	3.17	6.46
DE-FAKE	98.86	82.99	80.84	56.04	98.18	97.87
DCT	99.17	23.86	75.75	32.64	88.69	61.13
UnivCLIP	97.63	89.39	93.12	93.45	95.35	89.69
UnivConv2B	99.97	65.44	82.17	41.85	97.00	97.54
CAMME	99.65	91.36	96.05	99.12	98.70	97.91



Figure 3: Examples of various natural perturbations analyzed in our study.

comparing their feature distributions to real images. Higher FID scores indicate more significant perturbations. Results are summarized in Table 6.

Gaussian Noise Gaussian noise involves adding random pixel variations based on a Gaussian distribution. In this experiment, the mean was set to 0, and the standard deviation (σ) was varied as $\{0.01, 0.015, 0.02\}$.

Gaussian Blur Gaussian blur reduces noise or smooths edges by applying a Gaussian function:

$$G(x, y) = \frac{1}{2\pi\sigma^2} \exp\left(-\frac{x^2 + y^2}{2\sigma^2}\right), \quad (15)$$

where x and y are pixel coordinates, and σ determines blur intensity. Values of σ were tested from $\{0.5, 1.0, 1.5\}$.

JPEG Compression JPEG compression’s impact on deepfake detection was evaluated by varying the quality factor, representing compression intensity, across $\{30, 60, 90\}$. Higher quality factors result in less compression and better image fidelity [54, 55].

Sharpening Sharpening enhances image details by increasing the contrast between adjacent pixels. Experiments were conducted with sharpening factors of $\{1.0, 1.5, 2.0\}$.

Color Jittering Color jittering, a common augmentation technique, alters image properties like brightness, contrast, saturation, and hue. This experiment

focused on brightness and contrast. We used tune the same values for both from $\{1.0, 1.5, 2.0\}$.

Table 6 highlights the robustness of different methods under various natural perturbations. CAMME consistently outperforms other methods, maintaining high F1 scores across all perturbations, including Gaussian noise (91.36%), Gaussian blur (96.05%), and JPEG compression (99.12%). This demonstrates CAMME’s ability to effectively handle transformations that degrade image quality, as reflected in the FID values. In contrast, methods like DCT showed significant vulnerabilities (23.86% on Gaussian noise), while UnivCLIP and UnivConv2B performed competitively in certain scenarios, such as Gaussian blur (93.12%) and sharpening (97.00%), but fell short under more challenging transformations. The FID values indicate that transformations like color jittering (6.46) or Gaussian blur (4.40) introduce moderate perceptual degradation. However, the high F1 scores achieved by CAMME under these perturbations demonstrate its robustness to natural image transformations, highlighting its potential for detecting deepfakes in real-world scenarios.

5.4.4 Resilience to Adversarial Attacks

In this section, we evaluate the robustness of CAMME and other deepfake detectors against adversarial perturbations. Two widely used adversarial attacks, Fast Gradient Sign Method (FGSM) [56] and Projected Gradient Descent (PGD) [57], are applied to generate adversarial examples from clean fake images. The GLIDE test dataset, consisting of 1,700 fake images, is used for this evaluation. Figure 7 in Appendix D illustrates examples of fake images before and after the

Table 7: Robustness performance (F1 score) against adversarial attacks.

Methods	Natural Accuracy	FGSM Attack Accuracy	PGD Attack Accuracy
DE-FAKE	98.86	0.00	0.00
UnivCLIP	97.63	43.04	21.43
UnivConv2B	99.97	66.56	66.68
DCT	99.20	2.31	0.00
CAMME	99.65	96.14	89.01

adversarial attacks.

Attack Selection. FGSM is a one-step attack that perturbs the input image in the direction of the gradient of the loss function with respect to the input. In contrast, PGD generates adaptive adversaries by iteratively refining perturbations using the model’s gradients, resulting in a more tailored and robust attack against the target model. Both are widely studied white-box attacks, assuming the attacker has full access to the detector model’s architecture and parameters. The formula for FGSM is given by:

$$x_{\text{adv}} = x + \epsilon \cdot \text{sign}(\nabla_x \mathcal{L}(f(x; \phi), y)) \quad (16)$$

where x is the input image, x_{adv} is the adversarial image, ϵ is the perturbation strength, \mathcal{L} is the loss function, f is the detector model parametrized by ϕ , and y is the target label. On the other hand, PGD is a multi-step iterative attack that optimizes the objective function over multiple steps and projects each step (t) back within the ϵ -ball $B_\epsilon(x) = \{x' : \|x' - x\|_\infty \leq \epsilon\}$.

$$x_{\text{adv}}^{t+1} = \text{Proj}_{B_\epsilon(x)}(x_{\text{adv}}^t + \alpha \cdot \text{sign}(\nabla_x \mathcal{L}(f(x_{\text{adv}}^t; \phi), y))), \quad (17)$$

where $x_{\text{adv}}^0 = x$. To run these attacks, for FGSM, we set $\epsilon = 0.1$. For PGD, we set $\epsilon = 0.1$, $\alpha = 0.01$ and $t = 20$.

Results. Table 7 compares the robustness of various methods against selected attacks. The results demonstrate the strong performance of our proposed model, CAMME, in both generalization and resilience to adversarial perturbations. CAMME achieves a natural accuracy of 99.65%, showcasing its robust generalization on clean images, while UnivConv2B slightly outperforms it with 99.97%. However, CAMME excels under adversarial settings. Against FGSM attacks, CAMME achieves the highest F1 score of 96.14%, significantly surpassing UnivConv2B at 66.56%. Other methods, such as DE-FAKE and DCT, fail completely under FGSM attacks, with F1 scores of 0%.

For the more challenging PGD attacks, CAMME achieves an F1 score of 89.01%, representing a substantial improvement over UnivConv2B, the second-best

method, which scores 66.68%. Other methods, including UnivCLIP and DCT, show limited or no robustness, achieving 21.43% and 0.00%, respectively. These results highlight the limitations of baseline methods that rely on limited modalities or simple embeddings, making them vulnerable to adversarial perturbations. In contrast, CAMME’s integration of visual, textual, and frequency-domain embeddings enables it to capture richer input representations, significantly enhancing its robustness.

Overall, CAMME demonstrates strong generalization on clean images and exceptional resilience to adversarial attacks, outperforming existing methods across all scenarios. Its ability to leverage multi-modal embeddings and cross-attention mechanisms plays a crucial role in achieving these results, highlighting its effectiveness as a robust deepfake detection model.

5.4.5 Single-Head vs. Multi-Head Cross-Attention

The number of attention heads is a key hyperparameter in transformer-based models, as it governs the model’s ability to capture complex interactions between embeddings. Table 8 shows the performance of our model across inter-domain tasks as the number of attention heads H is varied in $\{1, 2, 4, 8, 16\}$. The results (in F1 score) indicate a consistent improvement in inter-domain performance as the number of heads increases, reaching the highest average performance of 72.73% when $H = 8$. For instance, at $H = 1$, the inter-domain average (IA) is 69.05%, which steadily increases to 69.09% at $H = 2$, 68.45% at $H = 4$, and peaks at $H = 8$ with 72.73%. However, a slight decline to 71.59% is observed when the number of heads is increased to 16. The optimal performance at $H = 8$ can be attributed to the model’s ability to strike a balance between adequately capturing the relationships across embeddings and maintaining computational efficiency. With fewer heads, such as $H = 1$, the model struggles to capture enough diverse interactions, leading to lower detection accuracy. On the other hand, while increasing the number of heads to $H = 16$ adds more capacity to model interactions, it introduces redundancy and potential overfitting, slightly degrading performance. Based on these results, we recommend setting the number of attention heads to $H = 8$, as it provides the best balance between complexity and performance, effectively capturing multi-modal interactions and enhancing detection transferability.

5.4.6 Impact of Input Image Size

This section analyzes the effect of input image size on the detection performance of our proposed model. Ta-

Table 8: Ablation study on varying the number of attention heads (intra-domain performance shown in bold blue text).

Number of Heads	Target		SD V1.5	ADM	GLIDE	VQDM	BigGAN	Inter-domain Average (IA)
	Source							
1	BigGAN		66.83	68.97	69.93	70.48	99.82	69.05
2	BigGAN		66.43	69.39	69.20	71.32	99.65	69.09
4	BigGAN		66.47	69.23	67.95	70.13	99.82	68.45
8	BigGAN		67.08	70.48	74.94	78.40	99.76	72.73
16	BigGAN		67.68	71.32	73.77	73.59	99.35	71.59

Table 9: Detection transferability performance across different input image sizes (intra-domain performance highlighted in bold blue text).

Methods	Target		SD V1.5	ADM	GLIDE	VQDM	BigGAN	Inter-domain Avg (IA)	Avg IA
	Source								
32 × 32	SD V1.5		91.37	66.60	71.08	68.98	67.46	68.53	68.12
	BigGAN		67.69	67.20	67.62	68.30	80.66	67.70	
64 × 64	SD V1.5		94.32	66.51	71.60	68.27	66.61	68.25	69.51
	BigGAN		67.45	70.87	77.78	66.94	94.48	70.76	
128 × 128	SD V1.5		95.28	65.70	78.79	67.95	66.68	69.78	68.26
	BigGAN		66.67	66.67	66.83	66.77	99.73	66.74	
224 × 224	SD V1.5		97.80	66.57	81.01	66.12	67.30	70.25	70.98
	BigGAN		68.20	67.44	84.14	67.05	98.27	71.71	
512 × 512	SD V1.5		98.33	73.82	84.97	80.13	72.13	77.76	74.08
	BigGAN		66.29	66.59	74.33	74.33	99.17	70.39	

ble 9 presents results across resolutions: 32×32 , 64×64 , 128×128 , 224×224 , and 512×512 , using images from BigGAN and Stable Diffusion (SD V1.5). Detection performance improves with larger resolutions, as higher spatial details enable better identification of subtle artifacts. For BigGAN, the best inter-domain performance is achieved at 224×224 with an F1 score of 71.71% and an intra-domain F1 score of 98.27%. However, at 512×512 , inter-domain performance slightly decreases to 70.39%, potentially due to redundancy in spatial details. In contrast, SD V1.5 consistently benefits from increased resolution, peaking at 512×512 with an inter-domain F1 score of 77.76% and an intra-domain F1 score of 98.33%. The lowest performance for both models is observed at 32×32 , where critical spatial details are lost, resulting in F1 scores of 67.70% for BigGAN and 68.53% for SD V1.5. In summary, the highest inter-domain performance of 74.08% is achieved at 512×512 , demonstrating the importance of higher resolutions. Larger inputs enhance the model’s ability to capture spatial and spectral patterns, improving the effectiveness of frequency transformations like the Discrete Cosine Transform (DCT) and enabling more robust, transferable embeddings that enhance detection performance across diverse domains.

6 Conclusion

This paper introduces CAMME (Cross-Attention Multi-Modal Embeddings), a framework addressing the critical challenge of cross-domain generalization in deepfake detection. By dynamically integrating visual, textual, and frequency-domain features through multi-head cross-attention, CAMME establishes robust decision boundaries that effectively generalize to unseen generative architectures. Our extensive experiments across 41 transfer tasks demonstrate significant performance improvements over state-of-the-art methods: 12.56% on natural scenes and 13.25% on facial deep-fakes.

CAMME’s multi-modal approach provides inherent resilience against both natural and adversarial perturbations, maintaining over 91% accuracy under image transformations and achieving 96.14% and 89.01% F1 scores against FGSM and PGD attacks, respectively. These results confirm that cross-modal integration through attention mechanisms effectively mitigates the domain-specificity limitations of previous approaches.

The demonstrated generalization capabilities and robustness position CAMME as an effective countermea-

sure against the rapidly evolving landscape of generative AI technologies. Future work could explore extending this approach to video deepfakes and investigating self-supervised adaptation techniques for emerging generative architectures.

References

- [1] Robin Rombach, Andreas Blattmann, Dominik Lorenz, Patrick Esser, and Björn Ommer. High-resolution image synthesis with latent diffusion models. In Proceedings of the IEEE/CVF Conference on Computer Vision and Pattern Recognition (CVPR), pages 10684–10695, June 2022.
- [2] Aditya Ramesh, Prafulla Dhariwal, Alex Nichol, Casey Chu, and Mark Chen. Hierarchical text-conditional image generation with clip latents, April 2022.
- [3] Or Patashnik, Zongze Wu, Eli Shechtman, Daniel Cohen-Or, and Dani Lischinski. Styleclip: Text-driven manipulation of stylegan imagery. In 2021 IEEE/CVF international conference on computer vision (ICCV), pages 2065–2074, Montreal, QC, Canada, October 2021. IEEE.
- [4] Chitwan Saharia, William Chan, Saurabh Saxena, Lala Li, Jay Whang, Emily Denton, Seyed Kamyar Seyed Ghasemipour, Raphael Gontijo-Lopes, Burcu Karagol Ayan, Tim Salimans, Jonathan Ho, David J. Fleet, and Mohammad Norouzi. Photorealistic text-to-image diffusion models with deep language understanding. In Alice H. Oh, Alekh Agarwal, Danielle Belgrave, and Kyunghyun Cho, editors, Advances in Neural Information Processing Systems (NeurIPS), 2022.
- [5] Pavel Korshunov and Sebastien Marcel. Deepfakes: a new threat to face recognition? assessment and detection, December 2018.
- [6] Yisroel Mirsky and Wenke Lee. The creation and detection of deepfakes: A survey. ACM Computing Surveys, 54(1), 2021.
- [7] Thanh Thi Nguyen, Quoc Viet Hung Nguyen, Dung Tien Nguyen, Duc Thanh Nguyen, Thien Huynh-The, Saeid Nahavandi, Thanh Tam Nguyen, Quoc-Viet Pham, and Cuong M. Nguyen. Deep learning for deepfakes creation and detection: A survey. Computer Vision and Image Understanding (CVIU), 223:103525, 2022.
- [8] A. Elgammal, Bingchen Liu, Mohamed Elhoseiny, and Marian Mazzone. Can: Creative adversarial networks, generating "art" by learning about styles and deviating from style norms. In International Conference on Innovative Computing and Cloud Computing (ICICC), 2017.
- [9] Aaron van den Oord, Sander Dieleman, Heiga Zen, Karen Simonyan, Oriol Vinyals, Alex Graves, Nal Kalchbrenner, Andrew Senior, and Koray Kavukcuoglu. Wavenet: A generative model for raw audio. In 9th ISCA Workshop on Speech Synthesis Workshop (SSW 9), page 125, 2016.
- [10] Jan Kietzmann, Linda W. Lee, Ian P. McCarthy, and Tim C. Kietzmann. Deepfakes: Trick or treat? Business Horizons, 63(2):135–146, March 2020.
- [11] Zeyang Sha, Zheng Li, Ning Yu, and Yang Zhang. De-fake: Detection and attribution of fake images generated by text-to-image generation models. In Proceedings of the 2023 ACM SIGSAC Conference on Computer and Communications Security (CCS), page 3418–3432, New York, NY, USA, 2023. Association for Computing Machinery.
- [12] Utkarsh Ojha, Yuheng Li, and Yong Jae Lee. Towards universal fake image detectors that generalize across generative models. In Proceedings of the IEEE/CVF Conference on Computer Vision and Pattern Recognition (CVPR), pages 24480–24489, June 2023.
- [13] Sifat Muhammad Abdullah, Aravind Cheruvu, Shravya Kanchi, Taejoong Chung, Peng Gao, Murtuza Jadliwala, and Bimal Viswanath. An analysis of recent advances in deepfake image detection in an evolving threat landscape. In 2024 IEEE Symposium on Security and Privacy (SP), pages 91–109, 2024.
- [14] Jonas Ricker, Simon Damm, Thorsten Holz, and Asja Fischer. Towards the detection of diffusion model deepfakes, January 2024.
- [15] Ashish Vaswani, Noam Shazeer, Niki Parmar, Jakob Uszkoreit, Llion Jones, Aidan N Gomez, Łukasz Kaiser, and Illia Polosukhin. Attention is all you need. In I. Guyon, U. Von Luxburg, S. Bengio, H. Wallach, R. Fergus, S. Vishwanathan, and R. Garnett, editors, Advances in Neural Information Processing Systems (NeurIPS), volume 30. Curran Associates, Inc., 2017.
- [16] Mingjian Zhu, Hanting Chen, Qiangyu YAN, Xudong Huang, Guanyu Lin, Wei Li, Zhijun Tu,

- Hailin Hu, Jie Hu, and Yunhe Wang. Genimage: A million-scale benchmark for detecting AI-generated image. In Thirty-seventh Conference on Neural Information Processing Systems (NeurIPS) Datasets and Benchmarks Track, 2023.
- [17] Danielle Citron and Robert Chesney. Deep fakes: a looming challenge for privacy, democracy, and national security. California Law Review (CLR), 107(6):1753, December 2019.
- [18] Luisa Verdoliva. Media forensics and deepfakes: An overview. IEEE Journal of Selected Topics in Signal Processing (JSTSP), 14(5):910–932, August 2020.
- [19] Momina Masood, Mariam Nawaz, Khalid Mahmood Malik, Ali Javed, Aun Irtaza, and Hafiz Malik. Deepfakes generation and detection: state-of-the-art, open challenges, countermeasures, and way forward. Applied Intelligence, 53(4):3974–4026, February 2023.
- [20] Xinsheng Xuan, Bo Peng, Wei Wang, and Jing Dong. On the generalization of gan image forensics. In Biometric Recognition, pages 134–141, Cham, 2019. Springer International Publishing.
- [21] Sheng-Yu Wang, Oliver Wang, Richard Zhang, Andrew Owens, and Alexei A. Efros. Cnn-generated images are surprisingly easy to spot... for now. In 2020 IEEE/CVF conference on computer vision and pattern recognition (CVPR), pages 8692–8701, Seattle, WA, USA, June 2020. IEEE.
- [22] Xin Wang, Nicolas Thome, and Matthieu Cord. Gaze latent support vector machine for image classification improved by weakly supervised region selection. Pattern Recognition, 72:59–71, December 2017.
- [23] Shuang Bai. Growing random forest on deep convolutional neural networks for scene categorization. Expert Systems with Applications, 71:279–287, April 2017.
- [24] Lilei Zheng, Stefan Duffner, Khalid Idrissi, Christophe Garcia, and Atilla Baskurt. Siamese multi-layer perceptrons for dimensionality reduction and face identification. Multimedia Tools and Applications, 53:3974–4026, 2015.
- [25] Huy H. Nguyen, Fuming Fang, Junichi Yamagishi, and Isao Echizen. Multi-task learning for detecting and segmenting manipulated facial images and videos. In 2019 IEEE 10th International Conference on Biometrics Theory, Applications and Systems (BTAS), page 1–8. IEEE Press, 2019.
- [26] Tianfei Zhou, Wenguan Wang, Zhiyuan Liang, and Jianbing Shen. Face forensics in the wild. In Proceedings of the IEEE/CVF Conference on Computer Vision and Pattern Recognition (CVPR), pages 5778–5788, June 2021.
- [27] Alec Radford, Jong Wook Kim, Chris Hallacy, Aditya Ramesh, Gabriel Goh, Sandhini Agarwal, Girish Sastry, Amanda Askell, Pamela Mishkin, Jack Clark, Gretchen Krueger, and Ilya Sutskever. Learning transferable visual models from natural language supervision. In Proceedings of the 38th international conference on machine learning (ICML), pages 8748–8763. PMLR, July 2021.
- [28] Junnan Li, Dongxu Li, Caiming Xiong, and Steven Hoi. Blip: Bootstrapping language-image pre-training for unified vision-language understanding and generation. In Proceedings of the 39th international conference on machine learning (ICML), pages 12888–12900. PMLR, June 2022.
- [29] Xiaofeng Wang, Kemu Pang, Xiaorui Zhou, Yang Zhou, Lu Li, and Jianru Xue. A visual model-based perceptual image hash for content authentication. IEEE Transactions on Information Forensics and Security, 10(7):1336–1349, 2015.
- [30] Basna Mohammed Salih Hasan, Siddeeq Y. Ameen, and Omer Mohammed Salih Hasan. Image authentication based on watermarking approach: Review. Asian Journal of Research in Computer Science (AJRCOS), 9(3):34–51, Jun. 2021.
- [31] Qichao Ying, Zhenxing Qian, Hang Zhou, Haisheng Xu, Xinpeng Zhang, and Siyi Li. From image to image: Immunized image generation. In Proceedings of the 29th ACM International Conference on Multimedia (MM), page 3565–3573, New York, NY, USA, 2021. Association for Computing Machinery.
- [32] Qichao Ying, Hang Zhou, Zhenxing Qian, Sheng Li, and Xinpeng Zhang. Learning to immunize images for tamper localization and self-recovery. IEEE Transactions on Pattern Analysis and Machine Intelligence (TPAMI), 45(11):13814–13830, 2023.
- [33] Bang An, Mucong Ding, Tahseen Rabbani, Aakriti Agrawal, Yuancheng Xu, Chenghao Deng, Sicheng Zhu, Abdirisak Mohamed, Yuxin Wen, Tom Goldstein, and Furong Huang.

- Waves: benchmarking the robustness of image watermarks. In Proceedings of the 41st International Conference on Machine Learning (ICML). JMLR.org, 2024.
- [34] Ian Goodfellow, Jean Pouget-Abadie, Mehdi Mirza, Bing Xu, David Warde-Farley, Sherjil Ozair, Aaron Courville, and Yoshua Bengio. Generative adversarial nets. In Z. Ghahramani, M. Welling, C. Cortes, N. Lawrence, and K.Q. Weinberger, editors, Advances in Neural Information Processing Systems (NeurIPS), volume 27. Curran Associates, Inc., 2014.
- [35] Yunjey Choi, Minje Choi, Munyoung Kim, Jung-Woo Ha, Sunghun Kim, and Jaegul Choo. StarGAN: Unified generative adversarial networks for multi-domain image-to-image translation. In 2018 IEEE/CVF conference on computer vision and pattern recognition (CVPR), pages 8789–8797, Salt Lake City, UT, June 2018. IEEE.
- [36] Tero Karras, Timo Aila, Samuli Laine, and Jaakko Lehtinen. Progressive growing of GANs for improved quality, stability, and variation. In International Conference on Learning Representations (ICLR), 2018.
- [37] Andrew Brock, Jeff Donahue, and Karen Simonyan. Large scale GAN training for high fidelity natural image synthesis. In International Conference on Learning Representations (ICLR), 2019.
- [38] Jonathan Ho, Ajay Jain, and Pieter Abbeel. Denoising diffusion probabilistic models. In Advances in neural information processing systems (NeurIPS), volume 33, pages 6840–6851. Curran Associates, Inc., 2020.
- [39] Prafulla Dhariwal and Alexander Nichol. Diffusion models beat gans on image synthesis. In Advances in neural information processing systems (NeurIPS), volume 34, pages 8780–8794. Curran Associates, Inc., 2021.
- [40] Alexander Quinn Nichol, Prafulla Dhariwal, Aditya Ramesh, Pranav Shyam, Pamela Mishkin, Bob McGrew, Ilya Sutskever, and Mark Chen. Glide: Towards photorealistic image generation and editing with text-guided diffusion models. In Proceedings of the 39th international conference on machine learning (ICML), pages 16784–16804. PMLR, June 2022.
- [41] Shuyang Gu, Dong Chen, Jianmin Bao, Fang Wen, Bo Zhang, Dongdong Chen, Lu Yuan, and Baining Guo. Vector quantized diffusion model for text-to-image synthesis. In 2022 IEEE/CVF conference on computer vision and pattern recognition (CVPR), pages 10686–10696, New Orleans, LA, USA, June 2022. IEEE.
- [42] N. Ahmed, T. Natarajan, and K.R. Rao. Discrete cosine transform. IEEE Transactions on Computers (TC), C-23(1):90–93, January 1974.
- [43] K. R. Rao and P. Yip. Discrete cosine transform: algorithms, advantages, applications. Academic Press Professional, Inc., USA, July 1990.
- [44] G.K. Wallace. The jpeg still picture compression standard. IEEE Transactions on Consumer Electronics (TCE), 38(1):xviii–xxxiv, 1992.
- [45] laion/clip-convnext_large_d.320.laion2b-s29b-b131k-ft-soup · hugging face, September 2023.
- [46] Jia Deng, Wei Dong, Richard Socher, Li-Jia Li, Kai Li, and Li Fei-Fei. Imagenet: A large-scale hierarchical image database. In 2009 IEEE conference on computer vision and pattern recognition (CVPR), pages 248–255, June 2009.
- [47] Zhiqing Guo, Gaobo Yang, Jiyou Chen, and Xingming Sun. Fake face detection via adaptive manipulation traces extraction network. Computer Vision and Image Understanding (CVIU), 204:103170, 2021.
- [48] Ziwei Liu, Ping Luo, Xiaogang Wang, and Xiaoou Tang. Deep Learning Face Attributes in the Wild . In 2015 IEEE International Conference on Computer Vision (ICCV), pages 3730–3738, Los Alamitos, CA, USA, December 2015. IEEE Computer Society.
- [49] Andreas Rossler, Davide Cozzolino, Luisa Verdoliva, Christian Riess, Justus Thies, and Matthias Niessner. FaceForensics++: Learning to Detect Manipulated Facial Images . In 2019 IEEE/CVF International Conference on Computer Vision (ICCV), pages 1–11, Los Alamitos, CA, USA, November 2019. IEEE Computer Society.
- [50] Durk P Kingma and Prafulla Dhariwal. Glow: Generative flow with invertible 1x1 convolutions. In Advances in neural information processing systems (NeurIPS), volume 31. Curran Associates, Inc., 2018.
- [51] Justus Thies, Michael Zollhöfer, Marc Stamminger, Christian Theobalt, and Matthias Nießner. Face2face: real-time face capture and reenactment of rgb videos. Communications of the ACM (CACM), 62(1):96–104, December 2018.

- [52] Diederik P. Kingma and Jimmy Ba. Adam: A method for stochastic optimization. In Yoshua Bengio and Yann LeCun, editors, 3rd International Conference on Learning Representations, ICLR 2015, San Diego, CA, USA, May 7-9, 2015, Conference Track Proceedings, 2015.
- [53] Martin Heusel, Hubert Ramsauer, Thomas Unterthiner, Bernhard Nessler, and Sepp Hochreiter. Gans trained by a two time-scale update rule converge to a local nash equilibrium. In I. Guyon, U. Von Luxburg, S. Bengio, H. Wallach, R. Fergus, S. Vishwanathan, and R. Garnett, editors, Advances in Neural Information Processing Systems (NeurIPS), volume 30. Curran Associates, Inc., 2017.
- [54] W.-L. Lau, Z.-L. Li, and K. W.-K. Lam. Effects of jpeg compression on image classification. International Journal of Remote Sensing, 24(7):1535–1544, 2003.
- [55] Genki Hamano, Shoko Imaizumi, and Hitoshi Kiya. Effects of jpeg compression on vision transformer image classification for encryption-then-compression images. Sensors, 23(3400), 2023.
- [56] Ian Goodfellow, Jonathon Shlens, and Christian Szegedy. Explaining and harnessing adversarial examples. In Yoshua Bengio and Yann LeCun, editors, 3rd International Conference on Learning Representations (ICLR), San Diego, CA, USA, May 7-9, 2015.
- [57] Aleksander Madry, Aleksandar Makelov, Ludwig Schmidt, Dimitris Tsipras, and Adrian Vladu. Towards deep learning models resistant to adversarial attacks. In International Conference on Learning Representations (ICLR), 2018.

A Dataset Details

In this section, we describe the dataset split used in our study. The Natural Scene dataset comprises images generated by various models, including SD V1.5, ADM, GLIDE, VQDM, and BigGAN, while the Face dataset consists of different real-fake combinations: CelPG, CelStar, CelGlow, and YouFace. Table 10 presents the dataset composition for both the Natural Scene and Face datasets.

Images in the Natural Scene dataset are grouped into 100 categories, specifically chosen from the first 100 categories in ImageNet [46]. In contrast, the Face

dataset features a diverse set of images that are not grouped into specific categories. For the Face dataset, we define the real and fake image combinations as follows:

- *CelPG*: CelebA-HQ (real) and PGGAN (fake)
- *CelStar*: CelebA (real) and StarGAN (fake)
- *CelGlow*: CelebA (real) and Glow (fake)
- *YouFace*: Youtube-Frame (real) and Face2Face (fake)

These combinations ensure a balanced dataset with consistent characteristics across realistic and synthetic face pairs, enhancing robustness in deepfake detection. Figure 4 provide examples of real and fake images from the Natural Scene and Face datasets, respectively.

B Detailed Results on Natural Scene and Face Datasets

In this section, we present the full results for deepfake detection performance on the Natural Scene and Face datasets. Table 11 provides the precision, recall, F1 score, and accuracy for each model on the Natural Scene dataset. Similarly, Table 12 presents the performance metrics for the Face dataset. The inter-domain average (IA) and the average of IA are also included for each model. The results demonstrate the effectiveness of our proposed model in enhancing cross-domain transferability and robustness in deepfake detection, particularly in the challenging Face dataset.

C Investigation of Fail Cases

As discussed in Section 5.3.2, we investigate the misalignment between visual and textual content in the YouFace dataset. The results are illustrated in Figure 5. YouFace is a particularly challenging dataset, combining real images with varying lighting conditions, poses, and expressions from YouTube-Frame [49], alongside advanced reenactment manipulations from Face2Face [51]. Additionally, the YouTube-Frame dataset contains repetitive content, such as a person speaking in front of a camera across multiple frames of the same video. This repetition confuses BLIP [28], making it difficult to generate precise captions that accurately capture the semantic meaning of the images. For instance, the caption generated for the first image in Figure 5 is “a woman with a necklace on a table”. However, neither a necklace nor a table is present in the image.

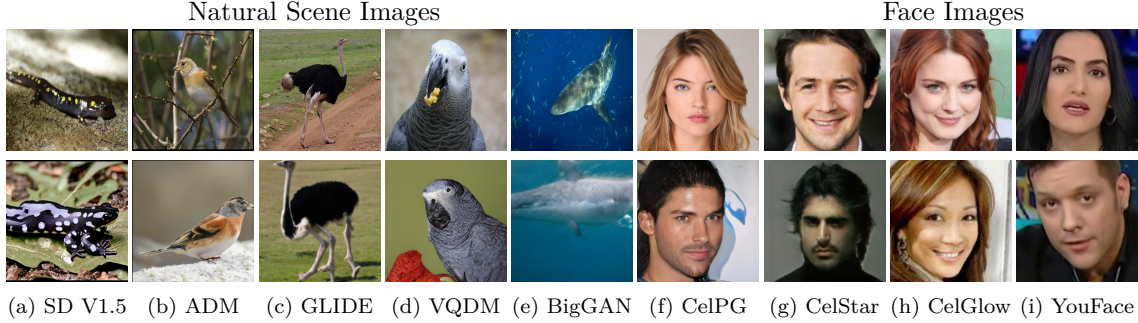


Figure 4: Sample image pairs (real/fake) from different generative models. Top: real images; bottom: synthetic. Left: natural scenes; Right: face generators.



Figure 5: Investigation of misalignment between visual and text content in the YouFace dataset.

Table 10: Dataset composition for Natural Scene and Face Datasets. Each dataset lists the number of fake and real images used in the training, validation, and test sets.

Dataset Type	Datasets	Train (Fake/Real)	Validation (Fake/Real)	Test (Fake/Real)
Natural Scene	SD V1.5	12,898/12,900	1,600/1,600	1,699/1,700
	ADM	12,837/12,837	1,591/1,591	1,692/1,692
	GLIDE	12,900/12,900	1,600/1,600	1,700/1,700
	VQDM	12,900/12,900	1,600/1,600	1,700/1,700
	BigGAN	12,900/12,900	1,600/1,600	1,700/1,700
Face	CelPG	8,000/8,000	1,000/1,000	1,000/1,000
	CelStar	8,000/8,000	1,000/1,000	1,000/1,000
	CelGlow	8,000/8,000	1,000/1,000	1,000/1,000
	YouFace	8,000/8,000	1,000/1,000	1,000/1,000

Such inconsistencies lead to ineffective alignment and weakened interactions between textual, visual, and frequency embeddings in our proposed model. This misalignment—whether between visual and textual embeddings or between textual and frequency embeddings—causes a drop in detection performance on the YouFace dataset. A potential solution to this issue is to improve the quality of text embeddings by training a more robust BLIP model on a larger and more diverse dataset. Alternatively, exploring specialized image-to-text generation models tailored for facial content may offer a more effective alignment mechanism in the future.

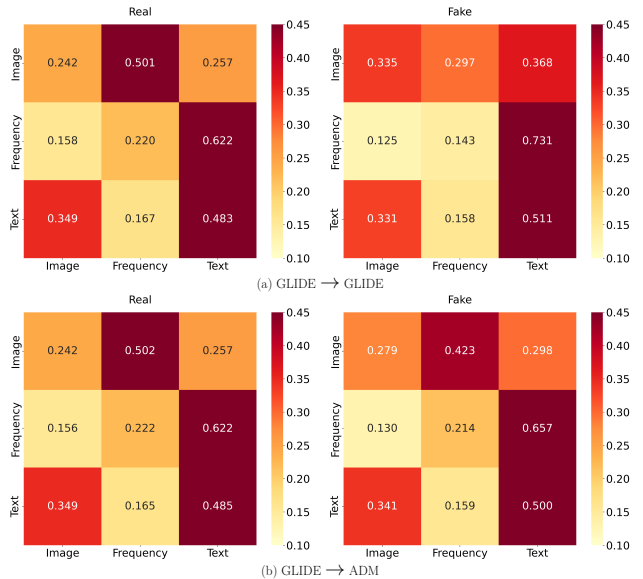


Figure 6: Visualization of attention matrices on the GLIDE and ADM datasets.

D Examples of Adversarial Images

Figure 7 presents examples of our original fake images, adversarial images generated using the FGSM attack, and those produced by the PGD attack.

Table 11: Precision / Recall / F1 / Accuracy scores (%) for deepfake detection performance on the Natural Scene dataset. Bold blue text indicates intra-domain performance. The highest F1 score is highlighted in bold, and the second-highest is underlined.

Methods	Target		SD V1.5		ADM		GLIDE		VQDM		BigGAN		Inter-domain Average (IA)	Average of IA	
	Source	Target	Source	Target	Source	Target	Source	Target	Source	Target	Source	Target			
DE-FAKE	SD V1.5	98.65 / 98.60 / 98.62 / 98.62			39.53 / 01.00 / 01.96 / 49.73		97.13 / 35.82 / 92.34 / 67.38		92.21 / 12.53 / 22.06 / 55.74		76.86 / 03.88 / 07.39 / 51.32		76.18 / 13.31 / 20.94 / 56.04	82.16 / 24.86 / 33.29 / 61.32	
	ADM	36.17 / 00.96 / 01.86 / 49.63	98.01 / 99.05 / 98.53 / 98.52			78.18 / 07.59 / 13.83 / 52.74		61.54 / 02.35 / 04.53 / 50.44		89.78 / 16.53 / 27.92 / 57.32		66.42 / 06.88 / 12.04 / 52.53			
	GLIDE	94.99 / 27.70 / 42.89 / 63.12	88.58 / 16.96 / 28.47 / 57.39	98.26 / 99.47 / 98.86 / 98.85			91.84 / 21.18 / 34.42 / 59.65		97.99 / 01.71 / 94.74 / 94.91		93.35 / 33.39 / 50.13 / 68.77		83.09 / 33.11 / 46.88 / 64.83		
	VQDM	81.16 / 22.02 / 34.64 / 58.46	72.81 / 13.77 / 23.16 / 54.31	86.05 / 36.65 / 51.40 / 65.35			94.62 / 96.29 / 95.45 / 95.41		92.33 / 68.00 / 78.32 / 81.18		83.09 / 33.11 / 46.88 / 64.83		83.09 / 33.11 / 46.88 / 64.83		
UnivCLIP	BigGAN	80.43 / 02.08 / 04.05 / 50.79	92.63 / 15.60 / 26.71 / 57.18	99.15 / 88.82 / 93.70 / 94.03			94.88 / 12.00 / 21.31 / 55.68		99.30 / 99.94 / 99.62 / 99.62		91.77 / 29.63 / 36.44 / 64.42		77.66 / 21.07 / 30.54 / 58.96	84.30 / 32.16 / 41.53 / 64.31	
	SD V1.5	96.47 / 98.37 / 97.41 / 97.39		56.14 / 03.78 / 07.09 / 50.41		92.88 / 50.65 / 65.55 / 73.38		72.25 / 8.12 / 14.60 / 52.50		89.35 / 21.71 / 34.93 / 59.56		77.66 / 21.07 / 30.54 / 58.96			
	ADM	42.45 / 05.84 / 10.27 / 48.96	92.73 / 92.79 / 92.76 / 92.76			88.74 / 59.35 / 71.13 / 75.91		93.32 / 94.47 / 93.89 / 93.85		91.98 / 76.88 / 83.76 / 85.09		79.12 / 59.14 / 64.76 / 75.95			
	GLIDE	92.77 / 26.69 / 41.43 / 62.30	90.01 / 15.96 / 27.13 / 67.18	98.40 / 96.76 / 97.63 / 97.65			91.14 / 16.94 / 28.57 / 57.65		93.96 / 40.47 / 56.33 / 69.38		92.70 / 23.02 / 38.33 / 61.63		83.09 / 33.11 / 46.88 / 64.83		
UnivConv2B	VQDM	72.46 / 09.61 / 16.96 / 52.98	91.36 / 38.12 / 53.79 / 67.26	86.50 / 28.65 / 43.04 / 62.09			95.90 / 98.94 / 97.39 / 97.35		96.78 / 81.24 / 88.33 / 89.26		86.78 / 39.41 / 50.53 / 67.90		86.78 / 39.41 / 50.53 / 67.90	89.91 / 35.09 / 39.44 / 67.02	
	BigGAN	69.70 / 01.29 / 02.54 / 50.37	78.90 / 05.08 / 09.55 / 51.86	94.87 / 13.06 / 22.96 / 56.18			97.50 / 41.29 / 58.02 / 70.12		99.41 / 98.76 / 99.09 / 99.09		85.24 / 15.18 / 23.27 / 57.13		85.24 / 15.18 / 23.27 / 57.13		
	SD V1.5	99.89 / 99.83 / 99.86 / 99.86		50.00 / 00.06 / 00.12 / 50.00		98.32 / 06.88 / 12.86 / 53.38		100.0 / 00.76 / 01.52 / 50.38		97.56 / 02.35 / 04.60 / 51.15		86.47 / 02.51 / 04.78 / 51.23			
	ADM	46.67 / 00.39 / 00.78 / 49.97	99.53 / 99.88 / 99.71 / 99.70			99.23 / 99.00 / 99.12 / 99.12		99.11 / 98.71 / 98.91 / 98.91		99.47 / 100.0 / 99.74 / 99.74		86.12 / 74.53 / 74.64 / 86.94			
DCT	GLIDE	78.92 / 00.56 / 01.12 / 50.20	99.38 / 13.89 / 24.38 / 56.51	99.94 / 100.0 / 99.97 / 99.97			100.0 / 19.88 / 33.17 / 59.94		100.0 / 51.88 / 70.87 / 77.44		94.13 / 22.30 / 32.39 / 61.12		94.13 / 22.30 / 32.39 / 61.12	64.19 / 61.61 / 62.72 / 63.26	
	VQDM	85.42 / 02.30 / 04.49 / 50.96	99.08 / 82.92 / 90.28 / 91.08	99.73 / 65.00 / 78.70 / 82.41			99.65 / 99.88 / 99.76 / 99.76		99.43 / 92.00 / 95.57 / 95.74		89.12 / 60.56 / 67.26 / 80.05		89.12 / 60.56 / 67.26 / 80.05		
	BigGAN	92.31 / 01.35 / 02.66 / 50.62	98.95 / 05.56 / 10.52 / 52.75	100.0 / 14.06 / 24.65 / 57.03			99.77 / 25.06 / 40.06 / 62.50		99.88 / 100.0 / 99.94 / 99.94		97.76 / 11.51 / 19.47 / 55.73		97.76 / 11.51 / 19.47 / 55.73		
	SD V1.5	95.86 / 97.64 / 96.74 / 96.71		49.92 / 44.27 / 46.52 / 49.11		73.40 / 55.35 / 63.11 / 67.65		90.24 / 90.29 / 90.27 / 90.26		56.07 / 50.00 / 52.86 / 55.41		67.18 / 59.98 / 63.19 / 65.61			
CAMME	ADM	63.69 / 83.26 / 72.17 / 67.89	99.41 / 99.00 / 99.20 / 99.20			56.60 / 72.12 / 63.42 / 58.41		65.81 / 81.06 / 72.64 / 69.47		47.07 / 56.29 / 51.27 / 46.50		58.29 / 73.18 / 64.88 / 60.57		58.29 / 73.18 / 64.88 / 60.57	68.68 / 99.35 / 79.94 / 70.71
	GLIDE	56.23 / 46.12 / 50.68 / 53.11	88.77 / 45.15 / 51.07 / 56.74	99.45 / 99.06 / 99.20 / 99.21			51.98 / 41.00 / 45.81 / 51.56		77.89 / 67.88 / 72.19 / 73.85		61.02 / 59.04 / 54.35 / 59.32		61.02 / 59.04 / 54.35 / 59.32		
	VQDM	87.10 / 84.94 / 86.01 / 86.18	78.23 / 69.68 / 73.71 / 75.15	78.30 / 54.76 / 64.45 / 69.79			96.37 / 98.29 / 97.32 / 97.29		96.37 / 98.29 / 97.32 / 97.29		84.14 / 27.41 / 36.77 / 61.44		80.19 / 69.55 / 72.74 / 76.33		
	BigGAN	58.06 / 56.07 / 57.04 / 57.78	66.60 / 59.87 / 63.06 / 64.92	95.01 / 98.53 / 96.74 / 96.68			60.41 / 54.29 / 57.19 / 59.35		100.0 / 100.0 / 100.0 / 100.0		70.02 / 67.19 / 68.51 / 69.68		70.02 / 67.19 / 68.51 / 69.68		
CAMME	SD V1.5	99.61 / 99.38 / 99.49 / 99.49		50.06 / 98.88 / 66.47 / 50.12		99.88 / 99.47 / 74.76 / 66.41		52.03 / 99.59 / 68.35 / 53.88		56.51 / 99.29 / 72.03 / 61.44		54.62 / 99.31 / 70.40 / 57.96		54.62 / 99.31 / 70.40 / 57.96	68.68 / 99.35 / 79.94 / 70.71
	ADM	49.73 / 98.93 / 66.19 / 49.47	99.88 / 99.05 / 99.47 / 99.47			92.52 / 99.00 / 95.65 / 95.50		99.12 / 98.82 / 98.97 / 98.97		99.47 / 99.06 / 99.26 / 99.26		85.21 / 98.95 / 96.02 / 85.80			
	GLIDE	57.33 / 99.94 / 66.94 / 56.66	83.13 / 99.82 / 69.33 / 55.88	99.59 / 99.71 / 99.65 / 99.65			88.09 / 99.71 / 73.41 / 63.88		88.94 / 99.87 / 74.12 / 65.15		55.12 / 99.83 / 70.96 / 58.89		55.12 / 99.83 / 70.96 / 58.89		
	VQDM	50.13 / 99.78 / 66.73 / 50.25	89.37 / 99.41 / 94.12 / 83.79	73.38 / 99.88 / 84.60 / 81.82			99.94 / 99.65 / 99.79 / 99.79		99.94 / 99.65 / 99.79 / 99.79		74.82 / 99.29 / 92.39 / 91.82		74.82 / 99.29 / 92.39 / 91.82		
CAMME	BigGAN	50.54 / 99.72 / 67.08 / 51.07	54.57 / 99.47 / 70.48 / 58.33	60.05 / 99.65 / 74.94 / 66.68			64.73 / 99.41 / 78.40 / 72.62		100.0 / 99.53 / 99.76 / 99.76		57.47 / 99.56 / 72.73 / 62.18		57.47 / 99.56 / 72.73 / 62.18		

Table 12: Precision / Recall / F1 / Accuracy scores (%) for deepfake detection performance on the Face dataset. Bold blue text indicates intra-domain performance. The highest F1 score is highlighted in bold, and the second-highest is underlined.

Methods	Target		CelPG		CelStar		CelGlow		YouFace		Inter-domain Average (IA)	Average of IA		
	Source	Target	Source	Target	Source	Target	Source	Target	Source	Target				
DE-FAKE	CelPG	99.36 / 92.70 / 95.91 / 96.05		96.91 / 47.00 / 63.30 / 72.75		71.15 / 03.70 / 07.03 / 51.10		100.0 / 00.80 / 01.59 / 50.40		89.35 / 17.17 / 23.97 / 58.08		89.35 / 17.17 / 23.97 / 58.08	57.65 / 13.65 / 15.98 / 52.16	
	CelStar	100.0 / 01.20 / 02.37 / 50.60	99.80 / 99.80 / 99.85 / 99.85			93.55 / 02.90 / 05.63 / 51.35		90.00 / 00.00 / 00.00 / 49.95		64.52 / 01.37 / 02.67 / 50.63		64.52 / 01.37 / 02.67 / 50.63		
	CelGlow	00.00 / 00.00 / 00.00 / 50.00	100.0 / 00.20 / 00.40 / 50.10	100.0 / 98.50 / 99.24 / 99.25			05.71 / 00.60 / 01.09 / 45.35		35.24 / 00.27 / 00.50 / 48.48		35.24 / 00.27 / 00.50 / 48.48			
	YouFace	61.28 / 73.90 / 67.00 / 63.60	54.39 / 31.00 / 39.49 / 52.50	95.80 / 89.00 / 92.28 / 92.55			08.77 / 02.50 / 03.89 / 38.25		71.97 / 91.90 / 80.72 / 78.05		41.48 / 35.80 / 36.79 / 51.45			41.48 / 35.80 / 36.79 / 51.45
UnivCLIP	CelPG	100.0 / 99.80 / 99.90 / 99.90		95.80 / 89.00 / 92.28 / 92.55		83.40 / 19.60 / 31.74 / 57.85		99.52 / 41.14 / 58.21 / 70.41		92.91 / 49.91 / 60.74 / 73.60		92.91 / 49.91 / 60.74 / 73.60	88.74 / 44.94 / 53.21 / 69.87	
	CelStar	100.0 / 62.64 / 77.03 / 81.31	99.70 / 98.80 / 99.25 / 99.25			91.18 / 03.10 / 06.00 / 51.40		99.61 / 25.60 / 40.73 / 62.67		96.93 / 30.45 / 41.25 / 65.13		96.93 / 30.45 / 41.25 / 65.13		
	CelGlow	89.74 / 03.50 / 06.73 / 51.52	94.48 / 58.20 / 72.03 / 77.40	96.70 / 99.50 / 99.88 / 99.85			68.21 / 20.52 / 31.55 / 55.39		84.14 / 27.41 / 36.77 / 61.44		84.14 / 27.41 / 36.77 / 61.44			
	YouFace	89.98 / 96.90 / 93.31 / 93.05	85.84 / 89.10 / 87.44 / 87.20	67.11 / 30.00 / 41.47 / 57.65			86.88 / 99.60 / 92.81 / 92.27		80.98 / 72.00 / 74.07 / 79.30		80.98 / 72.00 / 74.07 / 79.30			
UnivConv2B	CelPG	100.0 / 99.80 / 99.90 / 99.90		78.99 / 78.60 / 78.80 / 78.85		30.56 / 09.20 / 14.14 / 44.15		100.0 / 18.03 / 30.55 / 58.93		69.85 / 35.28 / 41.16 / 60.64		69.85 / 35.28 / 41.16 / 60.64	45.56 / 26.08 / 28.94 / 51.41	
	CelStar	00.00 / 00.00 / 00.00 / 49.98	100.0 / 99.90 / 99.95 / 99.95			00.00 / 00.00 / 00.00 / 50.00		00.00 / 00.00 / 00.00 / 00.50		00.00 / 00.00 / 00.00 / 33.49		00.00 / 00.00 / 00.00 / 33.49		
	CelGlow	57.14 / 00.40 / 00.79 / 50.02	100.0 / 50.70 / 67.29 / 75.35	100.0 / 100.0 / 100.0 / 100.0			47.17 / 27.39 / 34.66 / 48.25		68.10 / 26.16 / 34.25 / 57.87		68.10 / 26.16 / 34.25 / 57.87			
	YouFace	67.21 / 98.50 / 79.90 / 75.21	24.62 / 09.60 / 13.81 / 40.10	41.08 / 20.50 / 27.35 / 45.55			97.64 / 98.90 / 98.27 / 98.25		44.30 / 42.87 / 40.35 / 53.62		44.30 / 42.87 / 40.35 / 53.62			
DCT	CelPG	94.09 / 90.80 / 92.42 / 92.55		10.48 / 08.10 / 09.14 / 19.45		41.01 / 42.30 / 41.49 / 40.35		48.23 / 31.40 / 38.04 / 48.85		33.14 / 27.27 / 29.56 / 36.22		33.14 / 27.27 / 29.56 / 36.22	45.48 / 45.68 / 44.65 / 46.21	
	CelStar	34.03 / 35.70 / 34.85 / 33.25	99.80 / 100.0 / 99.95 / 99.95			73.50 / 43.00 / 54.26 / 63.75		50.29 / 68.30 / 57.93 / 50.40		52.61 / 49.00 / 49.01 / 49.13		52.61 / 49.00 / 49.01 / 49.13		
	CelGlow	44.28 / 44.90 / 44.59 / 44.20	24.71 / 17.10 / 20.21 / 32.50	99.20 / 99.50 / 99.95			48.42 / 59.60 / 53.43 / 48.05		39.14 / 40.53 / 39.41 / 41.58		39.14 / 40.53 / 39.41 / 41.58			
	YouFace	47.68 / 66.90 / 55.68 / 46.75	69.41 / 84.20 / 76.10 / 73.55	53.93 / 46.70 / 50.05 / 53.40			80.59 / 71.40 / 75.72 / 77.10		57.01 / 65.93 / 60.61 / 57.90		57.01 / 65.93 / 60.61 / 57.90			
CAMME	CelPG	99.90 / 99.60 / 99.75 / 99.75		65.06 / 89.00 / 75.17 / 70.60		47.85 / 89.00 / 62.24 / 46.00		54.64 / 100.0 / 70.67 / 58.50		55.85 / 92.67 / 69.36 / 58.37		55.85 / 92.67 / 69.36 / 58.37	56.15 / 86.88 / 66.46 / 55.96	
	CelStar	50.03 / 100.0 / 66.69 / 50.05	100.0 / 100.0 / 100.0 / 100.0			50.88 / 100.0 / 66.73 / 50.15		49.97 / 99.80 / 66.60 / 49.95		50.03 / 99.93 / 66.67 / 50.05		50.03 / 99.93 / 66.67 / 50.05		
	CelGlow	50.13 / 100.0 / 66.78 / 50.25	63.11 / 99.90 / 77.35 / 70.75	100.0 / 99.90 / 99.95 / 99.95			52.82 / 59.00 / 55.74 / 53.15		55.35 / 86.30 / 66.62 / 58.05		55.35 / 86.30 / 66.62 / 58.05			
	YouFace	94.63 / 61.70 / 74.70 / 79.10	45.87 / 72.10 / 56.07 / 43.50	49.62 / 72.10 /										

- Variation in Image-to-Frequency Attention:** Image-to-Frequency attention (row 1, column 2) shows significant differences between real and fake images. For instance, the attention weight is 0.501 for real images in the GLIDE \rightarrow GLIDE configuration, whereas it decreases to 0.297 for fake images. This indicates the model’s reliance on frequency-based details and textures that are characteristic of real images, which typically exhibit more complex and diverse frequency components. Conversely, for fake images, frequency information may be less informative or even misleading due to artifacts and inconsistencies, resulting in a lower Image-to-Frequency attention score when analyzing synthetic data.
- Role of Text Embeddings in Fake Images:** Text-to-Image attention (row 3, column 1) and Text Self-Attention (row 3, column 3) scores are consistently higher, highlighting the importance of text embeddings in capturing semantic information and guiding the model to focus on relevant visual features. Fake images from diffusion-based models, for instance, exhibit high Text Self-Attention scores (0.500), suggesting that these images may contain text-related artifacts or repetitive patterns that reinforce certain features within the Text embedding. This phenomenon could serve as a potential indicator for detecting Diffusion-generated fake images.
- Transferable Attention Map:** The similarity observed between attention matrices for different configurations (e.g., fake class in GLIDE \rightarrow GLIDE and GLIDE \rightarrow ADM) indicates a strong transferability of the model’s attention mechanism from the GLIDE to the ADM dataset. The model appears to rely on stable attention patterns, particularly in self-attention for Frequency and Text embeddings, which remain effective across datasets. Minor variations, such as a slightly higher Text-to-Text attention score in Stable diffusion-based fake images, suggest that the model can subtly adapt to different artifact types, enhancing its potential for generalization across generative models.

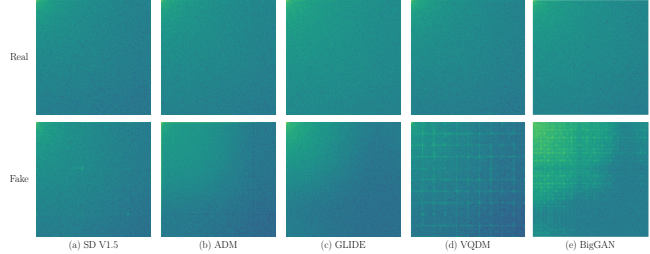


Figure 8: Average DCT spectrum of real (top row) and fake (bottom row) images generated by various models. Values are shown on a log scale and limited to the range $[-25, 5]$ for improved visualization.

1,700 images per class (see Table 10) and visualized after applying a logarithmic transformation. The results are shown in Figure 8.

Our observations indicate that diffusion-based models trained with classifier-free guidance (e.g., ADM, GLIDE) produce DCT spectra with smooth, continuous energy distributions, with high energy concentrated in the lower frequency bands (top-left corner), closely resembling the characteristics of real images. We attribute this to the influence of prompt conditioning, which enables these models to generate detailed, context-specific, and semantically rich images. This conditioning provides fine-grained control over the generated content and significantly reduces artifacts, resulting in more natural-looking images.

In contrast, the DCT spectra of GAN-generated images display a more fragmented energy distribution, with a noticeable spread into higher frequency bands. This distribution is influenced by factors such as single-step generation, mode collapse, and instability during GAN training. Additionally, the DCT spectra of VQDM (Vector Quantized Diffusion Model) reveal a grid-like pattern due to its use of discrete codebook embeddings to represent synthetic images. Through quantization, VQDM converts the continuous pixel space into discrete latent codes, which are then processed in the denoising steps, often resulting in regular, repeating high-frequency components. This spectral pattern reflects unnatural periodicity, frequently manifesting in the spatial domain as visible blockiness or repetitive artifacts.

F DCT spectra

In this section, we analyze the DCT spectra of real and fake images. Following [14], grayscale-converted test images are transformed using the Discrete Cosine Transform (DCT, (4)) to extract frequency components. The average DCT spectra are computed across